Extraction of the neutron magnetic form factor from quasielastic $^3\vec{\mathrm{He}}(\vec{e}, e')$ at $Q^2 = 0.1$–$0.6\,(\mathrm{GeV}/c)^2$

B. Anderson,[10] L. Auberbach,[18] T. Averett,[3] W. Bertozzi,[11] T. Black,[11,*] J. Calarco,[22] L. Cardman,[19] G. D. Cates,[14,†] Z. W. Chai,[11,‡] J. P. Chen,[19] Seonho Choi,[18,§] E. Chudakov,[19] S. Churchwell,[4,‖] G. S. Corrado,[14] C. Crawford,[11] D. Dale,[21] A. Deur,[20,¶] P. Djawotho,[3,**] D. Dutta,[11,††] J. M. Finn,[3] H. Gao,[11,††] R. Gilman,[16,19] A. V. Glamazdin,[9] C. Glashausser,[16] W. Glöckle,[15] J. Golak,[8] J. Gomez,[19] V. G. Gorbenko,[9] J.-O. Hansen,[19,‡‡] F. W. Hersman,[22] D. W. Higinbotham,[23,¶] R. Holmes,[17] C. R. Howell,[4] E. Hughes,[1] B. Humensky,[14,§§] S. Incerti,[18,‖‖] C. W. de Jager,[19] J. S. Jensen,[1,¶¶] X. Jiang,[16] C. E. Jones,[1,***] M. Jones,[3,¶] R. Kahl,[17] H. Kamada,[15,†††] A. Kievsky,[5] I. Kominis,[14] W. Korsch,[21] K. Kramer,[3,††] G. Kumbartzki,[16] M. Kuss,[19,‡‡‡] E. Lakuriqi,[18,§§§] M. Liang,[19] N. Liyanage,[19,†] J. LeRose,[19] S. Malov,[16] D. J. Margaziotis,[2] J. W. Martin,[11,‖‖‖] K. McCormick,[13,¶¶¶] R. D. McKeown,[1] K. McIlhany,[11,****] Z.-E. Meziani,[18] R. Michaels,[19] G. W. Miller,[14] J. Mitchell,[19,††††] S. Nanda,[19] E. Pace,[7] T. Pavlin,[1,‡‡‡‡] G. G. Petratos,[10] R. I. Pomatsalyuk,[9] D. Pripstein,[1,§§§§] D. Prout,[10] R. D. Ransome,[16] Y. Roblin,[20,¶] M. Rvachev,[11] A. Saha,[19] G. Salmè,[6] M. Schnee,[18] J. Seely,[11] T. Shin,[11,‖‖‖‖] K. Slifer,[18,†] P. A. Souder,[17] S. Strauch,[16,¶¶¶¶] R. Suleiman,[10,*****] M. Sutter,[11,†††††] B. Tipton,[11,‡‡‡‡‡] L. Todor,[13,§§§§§] M. Viviani,[5] B. Vlahovic,[12,19] J. Watson,[10] C. F. Williamson,[11] H. Witała,[8] B. Wojtsekhowski,[19] F. Xiong,[11,††††] W. Xu,[11,‖‖‖‖‖] J. Yeh,[17] and P. Żołnierczuk[21,**]

(Jefferson Lab E95-001 Collaboration)

[1]*California Institute of Technology, Pasadena, California 91125, USA*
[2]*California State University, Los Angeles, California 90032, USA*
[3]*College of William and Mary, Williamsburg, Virginia 23187, USA*
[4]*Duke University, Durham, North Carolina 27708, USA*
[5]*Istituto Nazionale di Fisica Nucleare, Sezione di Pisa, I-56100 Pisa, Italy*
[6]*Istituto Nazionale di Fisica Nucleare, Sezione di Roma, I-00185 Roma, Italy*
[7]*Università di Roma "Tor Vergata" and Istituto Nazionale di Fisica Nucleare, Sezione di Roma II, I-00133 Roma, Italy*
[8]*M. Smoluchowski Institute of Physics, Jagellonian University, PL-30059 Cracow, Poland*
[9]*Kharkov Institute of Physics and Technology, Kharkov 310108, Ukraine*
[10]*Kent State University, Kent, Ohio 44242, USA*
[11]*Massachusetts Institute of Technology, Cambridge, Massachusetts 02139, USA*
[12]*North Carolina Central University, Durham, North Carolina 27707, USA*
[13]*Old Dominion University, Norfolk, Virginia 23508, USA*
[14]*Princeton University, Princeton, New Jersey 08544, USA*
[15]*Ruhr-Universität Bochum, D-44780 Bochum, Germany*
[16]*Rutgers University, Piscataway, New Jersey 08855, USA*
[17]*Syracuse University, Syracuse, New York 13244, USA*
[18]*Temple University, Philadelphia, Pennsylvania 19122, USA*
[19]*Thomas Jefferson National Accelerator Facility, Newport News, Virginia 23606, USA*
[20]*Université Blaise Pascal/IN2P3, F-63177 Aubière, France*
[21]*University of Kentucky, Lexington, Kentucky 40506, USA*
[22]*University of New Hampshire, Durham, New Hampshire 03824, USA*
[23]*University of Virginia, Charlottesville, Virginia 22903, USA*

(Received 9 May 2006; revised manuscript received 22 November 2006; published 16 March 2007)

We have measured the transverse asymmetry $A_{T'}$ in the quasielastic $^3\vec{\mathrm{He}}(\vec{e}, e')$ process with high precision at Q^2 values from 0.1 to 0.6 $(\mathrm{GeV}/c)^2$. The neutron magnetic form factor G_M^n was extracted at Q^2 values of 0.1 and 0.2 $(\mathrm{GeV}/c)^2$ using a nonrelativistic Faddeev calculation which includes both final-state interactions (FSI) and meson-exchange currents (MEC). Theoretical uncertainties due to the FSI and MEC effects were constrained with a precision measurement of the spin-dependent asymmetry in the threshold region of $^3\vec{\mathrm{He}}(\vec{e}, e')$. We also extracted the neutron magnetic form factor G_M^n at Q^2 values of 0.3 to 0.6 $(\mathrm{GeV}/c)^2$ based on plane wave impulse approximation calculations.

DOI: 10.1103/PhysRevC.75.034003 PACS number(s): 13.40.Gp, 14.20.Dh, 24.70.+s, 25.10.+s

*Present address: University of North Carolina at Wilmington, Wilmington, North Carolina 28403, USA.

†Present address: University of Virginia, Charlottesville, Virginia 22903, USA.

‡Present address: Brookhaven National Laboratory, Upton, New York 11973, USA.

§Present address: Seoul National University, Seoul, 151-747 Korea.

‖Present address: University of Canterbury, Christchurch, New Zealand.

I. INTRODUCTION

The electromagnetic structure of the nucleon has long been a topic of fundamental interest in nuclear and particle physics. First-order nucleon electromagnetic properties are commonly parametrized in terms of elastic form factors [1]. At low values of four-momentum transfer squared, Q^2, these functions have a simple interpretation as the Fourier transforms of the nucleon charge and magnetization densities in the Breit frame. Their precise experimental determination is important both for testing fundamental theories of hadron structure and for the analysis of other experiments in the field, such as parity violation measurements [2,3] which are designed to probe the strangeness content of the nucleon.

The proton form factors have been determined with good precision at low Q^2 using Rosenbluth separation of elastic electron-proton cross sections, and more recently at higher Q^2 using a polarization transfer technique [4,5]. The neutron form factors are less well known because of the zero electric charge of the neutron, causing its electric form factor to be small, and experimental complications such as the lack of free neutron targets and difficulties associated with neutron detectors.

Over the past two decades, with the advent of much improved experimental facilities, the precise measurement of both the neutron electric form factor G_E^n and the magnetic form factor G_M^n has become a focus of activity. Until recently, most data on G_M^n had been deduced from elastic and quasielastic electron-deuteron scattering. Inclusive measurements of this type suffer from large theoretical uncertainties due in part to the deuteron model employed and in part to corrections for final-state interactions (FSI) and meson-exchange currents (MEC). The sensitivity to nuclear structure is reduced by measuring the neutron in coincidence, $^2\mathrm{H}(e, e'n)$ [6], and, further, by taking the ratio of cross sections of $^2\mathrm{H}(e, e'n)$ to $^2\mathrm{H}(e, e'p)$ at quasielastic kinematics [7–11]. Uncertainties of less than 2% in G_M^n have been achieved in the region $Q^2 < 1\,(\mathrm{GeV}/c)^2$ using the latter technique [10,11]. Despite this high precision, there is significant disagreement between the results of Refs. [6–8] and those of the more recent experiments [9–11] of up to 10% in the absolute value of G_M^n. An explanation has been suggested in Ref. [12], but the issue has remained contentious.

To clarify the situation experimentally, additional data on G_M^n, preferably obtained using a complementary method, are highly desirable. Inclusive quasielastic $^3\vec{\mathrm{He}}(\vec{e}, e')$ scattering provides such an alternative approach [13]. In contrast to deuterium experiments, this technique employs a different target and relies on polarization degrees of freedom. It is thus subject to completely different systematics. On the other hand, because of the more complex physics of the three-body system, the precise extraction of nucleon form factors from polarized ^{3}He measurements requires careful modeling of the nuclear structure and of the reaction mechanism. Recent advances in Faddeev calculations [14–16] have brought theoretical uncertainties of ^{3}He models sufficiently under control to allow such studies in the nonrelativistic kinematic regime. A precision comparable to that of the deuterium ratio experiments can be achieved using the polarized ^{3}He technique [17].

The use of polarized ^{3}He targets was pioneered at MIT-Bates [18–21] and Mainz [22]. In Ref. [20], G_M^n was extracted for the first time from quasielastic inclusive scattering from polarized ^{3}He, although with a large statistical uncertainty.

In this paper, we report on the first precision measurement of the so-called transverse asymmetry $A_{T'}$, which is sensitive to G_M^n, in the inclusive reaction $^3\vec{\mathrm{He}}(\vec{e}, e')$. The results were obtained in Hall A at the Thomas Jefferson National Accelerator Facility (Jefferson Lab). Brief reports of these data have appeared previously [17,23,24]. This paper presents the data analysis and evaluation of model uncertainties in much more detail. In addition, the analysis has been slightly refined. The results presented here are final.

The neutron magnetic form factor G_M^n was extracted at $Q^2 = 0.1$ to $0.6\,(\mathrm{GeV}/c)^2$ in steps of $0.1\,(\mathrm{GeV}/c)^2$ [17,23].

¶Present address: Thomas Jefferson National Accelerator Facility, Newport News, Virginia 23606, USA.
**Present address: Indiana University Cyclotron Facility, Bloomington, Indiana 47408, USA.
††Present address: Duke University, Durham, North Carolina 27708, USA.
‡‡ Corresponding author. Electronic mail address: ole@jlab.org
§§Present address: The Enrico Fermi Institute, University of Chicago, Chicago, Illinois 60637, USA.
‖‖Present address: IN2P3/CNRS, Université Bordeaux, F-33175 Gradignan Cedex, France.
¶¶Present address: Bookham Inc., San Jose, California 95134, USA.
***Present address: Siimpel Corp., Arcadia, California 91006, USA.
†††Present address: Kyushu Institute of Technology, Kitakyushu 804-8550, Japan.
‡‡‡ Present address: Istituto Nazionale di Fisica Nucleare, Sezione di Pisa, I-56100 Pisa, Italy.
§§§Present address: University of Pennsylvania, Philadelphia, Pennsylvania 19104, USA.
‖‖‖ Present address: University of Winnipeg, Winnipeg, Manitoba R3B 2E9, Canada, USA.
¶¶¶Present address: Pacific Northwest Laboratory, Richland, Washington 99352, USA.
****Present address: U.S. Naval Academy, Annapolis, Maryland 21402, USA.
††††Present address: Renaissance Technologies Inc., Stony Brook, New York 11790, USA.
‡‡‡‡ Present address: Center for Astrophysics, Harvard University, Cambridge, Massachusetts 02138, USA.
§§§§Present address: Harmonic Inc., Sunnyvale, California 94089, USA.
‖‖‖‖ Present address: Hampton University, Hampton, Virginia 23668, USA.
¶¶¶¶Present address: University of South Carolina, Columbia, South Carolina, 29208.
*****Present address: Virginia Polytechnic Institute, Blacksburg, Virginia 24061, USA.
†††††Present address: RightAnswers LLC, Clark, New Jersey 07066, USA.
‡‡‡‡‡ Present address: MIT-Lincoln Laboratory, Lexington, Massachusetts 02420, USA.
§§§§§Present address: Oblon, Spivak, McClelland, Maier & Neustadt, P. C., Alexandria, Virginia 22314.
‖‖‖‖‖Present address: Shanghai Institute of Applied Physics, Shanghai 201800, China.

In addition, high-precision asymmetry data in the ^{3}He breakup region were obtained at Q^2 values of 0.1 and 0.2 $(\mathrm{GeV}/c)^2$ [24]. The threshold data provide a stringent test of the above-mentioned Faddeev calculations because they cover a kinematical region where the proper treatment of the reaction mechanism is particularly important.

At the $Q^2 = 0.1$ and 0.2 $(\mathrm{GeV}/c)^2$ kinematics, G_M^n was extracted using a state-of-the-art Faddeev calculation [16]. At these low Q^2 values, relativistic effects are small, and the nonrelativistic Faddeev results have been shown to be in good agreement with a diverse set of few-body data, including our own ^{3}He breakup threshold data [24]. On the other hand, the extraction of G_M^n from our ^{3}He asymmetry data at higher values of Q^2 with the same precision as that achieved at low Q^2 would require a more advanced theory that includes both an accurate treatment of reaction mechanism effects (FSI and MEC) and proper relativistic corrections (and possibly other refinements, such as Δ-isobar excitations, presumed to be small at our kinematics). Unfortunately, such a comprehensive calculation is not available at the present time, and efforts to extend the theory are only in the beginning stages. For example, full inclusion of FSI has been investigated for the two-body channel in Ref. [25]. The Hannover group has carried out a coupled-channel calculation of $^3\vec{\mathrm{He}}(\vec{e}, e')$ that accounts for FSI and Δ isobars [26], but unfortunately also with limited success at higher Q^2. Nonetheless, we observe that the size of FSI and MEC corrections to inclusive scattering data near the top of the quasielastic peak has been predicted to diminish sharply with increasing momentum transfer [27–30]. Hence, it appears likely that the plane wave impulse approximation (PWIA), in which the knocked-out nucleon is described by a plane wave while the spectator pair is fully interacting, is reasonably accurate at the higher Q^2 values of this experiment. A quantitative estimate of the Q^2 behavior of deviations from the PWIA, in particular of the size of FSI corrections, could be obtained by performing a y-scaling analysis on the present ^{3}He asymmetry data [31]. Such an analysis may be carried out in a future publication.

Taking the pragmatic point of view that the PWIA is currently the best available theory describing inclusive quasielastic scattering from polarized ^{3}He at $Q^2 \geqslant 0.3\,(\mathrm{GeV}/c)^2$, we have extracted G_M^n from our higher Q^2 data [23] using PWIA. While we do not attempt to go beyond the PWIA by computing corrections for the various effects omitted in this approximation, we provide estimates of the uncertainties of the results in considerable detail. Despite the relatively large theoretical uncertainties in this approach, our results are in good agreement with the recent deuterium ratio measurements from Mainz [10,11] in the same Q^2 region.

II. THEORY

A. Spin-dependent inclusive electron scattering

Figure 1 depicts inclusive scattering of longitudinally polarized electrons from a polarized nuclear target. The four-momentum of the electrons before and after the reaction is $k = (E, \mathbf{k})$ and $k' = (E', \mathbf{k}')$, respectively. The four-momentum

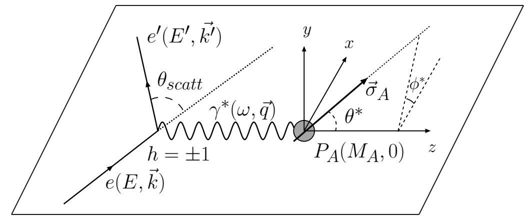

FIG. 1. Spin-dependent inclusive electron scattering from a polarized target. The target spin angles θ^* and ϕ^* are defined with respect to the three-momentum transfer vector $\mathbf{q}$.

transfer to the target is $q = k - k' = (\omega, \mathbf{q})$, with the usual definition $Q^2 \equiv -q^2$.

The experiment measured the spin-dependent asymmetry $A = (\sigma^+ - \sigma^-)/(\sigma^+ + \sigma^-)$, where $\sigma^\pm$ is the differential cross section for quasielastic scattering of electrons with helicity $h = \pm 1$ from polarized ^{3}He. It can be expressed in terms of nuclear response functions $R(Q^2, \omega)$ and kinematic factors $v(Q^2, \omega)$ as [32]

$$A = -\frac{\cos\theta^* \nu_{T'} R_{T'} + 2\sin\theta^* \cos\phi^* \nu_{\mathrm{TL}'} R_{\mathrm{TL}'}}{\nu_L R_L + \nu_T R_T}, \qquad (1)$$

where θ^* and ϕ^* are the polar and azimuthal angles of the target spin direction with respect to the three-momentum transfer vector $\mathbf{q}$, as shown in Fig. 1. By choosing $\theta^* = 0^\circ$ or $\theta^* = 90^\circ$, one can select the transverse asymmetry $A_{T'}$ or the longitudinal-transverse asymmetry $A_{\mathrm{TL}'}$.

The nuclear response functions for inclusive quasielastic scattering have been obtained through both PWIA and Faddeev calculations. These calculations will be discussed briefly next.

B. Plane wave impulse approximation

In the PWIA, it is assumed that a single nucleon within the target nucleus completely absorbs the momentum of the virtual photon and leaves the interaction region as a plane wave. The remaining two-nucleon subsystem still undergoes interaction. Exchange current effects are ignored. The target nucleus, in our case ^{3}He, however, is described by the solution of the Schrödinger equation with realistic nuclear forces. Relativistic effects are included by using relativistic energy conservation and a relativistic electron-nucleon cross section.

The nuclear current tensor is calculated as the product of the nucleonic current tensor and the nuclear spectral function, which contains the nuclear structure information (see, for example, Refs. [33–36]). The spin-independent part of the spectral function has the well-known interpretation as the probability of finding a nucleon of certain momentum and isospin in the target nucleus [37]. The PWIA formalism available in the literature is largely but not necessarily fully covariant.

Expressions for the matrix elements of the nucleonic current tensor and the spin-dependent nuclear spectral function have been derived in Ref. [36]. The spectral function can be computed numerically from the nuclear wave function, which in turn can be obtained from a model of the nucleon-nucleon (NN) potential. With the nucleonic current tensor and the nuclear spectral function at hand, expressions for the functions

$R(Q^2, \omega)$, required in Eq. (1), can be derived and evaluated numerically [36].

The PWIA results presented in the paper were calculated following Ref. [33]. The calculation was based on a ^{3}He wave function derived from the Argonne AV18 NN potential [38] and used the Höhler nucleon form factor parametrization [39].

C. Nonrelativistic Faddeev calculation

In the Faddeev approach [14], the coordinate-space Schrödinger equation for three nucleons with two-nucleon interactions is decomposed into three separate equations [40]. In momentum space, the three Faddeev equations can be written as three integral equations. The kernel in each equation involves only the interaction between one pair of nucleons. Solutions are obtained numerically. The Faddeev decomposition of the three-body (and four-body) problem has proven to be a very useful computational tool in studies of light nuclei.

With regard to ^{3}He, the Faddeev formalism has been applied to unpolarized pd and ppn electrodisintegration [15,41] with full inclusion of all final-state rescattering processes. This calculation was subsequently extended to electrodisintegration of polarized ^{3}He [42]. A further extension was made by including proper treatment of meson-exchange currents [16] according to the Riska prescription [43], which relates NN forces and meson-exchange currents in a model-independent manner through the continuity equation. In Ref. [16], only the dominant π- and ρ-like meson-exchange terms shown in Fig. 2 were considered. The effect of Δ currents has also been studied and found to be small (see Sec. V B).

The derivation of the nuclear response functions in the Faddeev approach is described further in Ref. [42]. In this work, the resulting expressions were evaluated numerically using the framework of Ref. [16] for a large number of kinematic points corresponding to the acceptance regions covered by the experiment. The underlying ^{3}He wave function was obtained using the BonnB NN potential [44]. Again, the Höhler parametrization [39] was used to model the nucleon elastic form factors. The Faddeev calculation does not include relativistic effects.

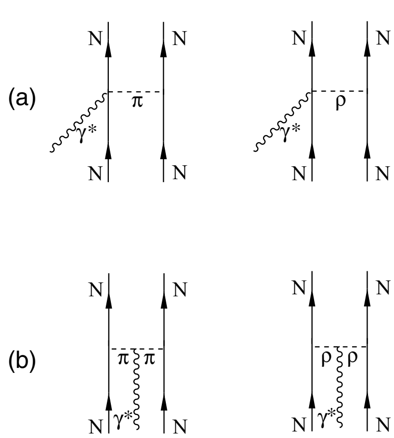

FIG. 2. MEC contributions included in the Faddeev calculation [16]. (a) Couplings to a correlated nucleon pair; (b) couplings to a π or ρ in flight.

D. Extraction of the neutron magnetic form factor

Because the ^{3}He nuclear spin is carried mainly by the neutron, the spin-dependent response functions $R_{T'}$ and $R_{TL'}$ can be expected to contain a large if not dominant neutron contribution at quasielastic kinematics [13]. Comparison of Eq. (1) with the corresponding expression for scattering from a free nucleon leads to the expectation (within PWIA) that

$$R_{T'} \propto P_n\left(G_M^n\right)^2 + P_p\left(G_M^p\right)^2, \tag{2}$$

$$R_{TL'} \propto P_n G_M^n G_E^n + P_p G_M^p G_E^p, \tag{3}$$

where P_n and P_p are the effective polarizations of the neutron and the protons, respectively, in ^{3}He. Because the proton spins largely cancel, we have $|P_p| \ll |P_n|$. Effective polarizations have been calculated, e.g., in Refs. [33,34,45]. Since $|G_M^n| \approx |G_M^p|$, the proton contribution to the transverse response $R_{T'}$ is small, and hence $R_{T'}$ is essentially proportional to $(G_M^n)^2$. Based on these arguments, the asymmetry $A_{T'}$ defined in Eq. (1) can be written as a function of the neutron magnetic form factor,

$$A_{T'}\left({G_M^n}^2\right) = \frac{1 + a\left(G_M^n\right)^2}{b + c\left(G_M^n\right)^2}, \tag{4}$$

where $|a| \gg 1$ and $b > c$ at low Q^2 where the above assumptions hold. By comparing $A_{T'}$ data with predictions for $A_{T'}$ from a calculation, one can extract G_M^n. The detailed procedure will be discussed in Sec. VI.

For completeness, we mention that because $|G_E^p| \gg |G_E^n|$, the proton contribution to the transverse-longitudinal response $R_{TL'}$ may be dominant despite the small effective proton polarization. Thus inclusive scattering from polarized ^{3}He is not a promising technique for measuring the neutron electric form factor G_E^n [21,46].

III. EXPERIMENT

A. Overview and kinematics

The experiment, E95-001, was performed in Hall A at Jefferson Lab using a continuous-wave electron beam of 15 μA current and 70% longitudinal polarization, incident on a high-pressure polarized ^{3}He gas target. The beam energies were 778 and 1727 MeV.

Electrons scattered from the target were detected by two high-resolution spectrometers (HRSs) positioned on the left- and right-hand sides of the beam line. Both spectrometers were configured for electron detection and independent operation (single-arm mode). The "electron spectrometer" on the left side of the beam performed the main physics measurement of inclusive $^3\vec{\mathrm{He}}(\vec{e}, e')$ scattering at six different quasielastic kinematics. The second HRS, the "hadron spectrometer" to the right of the beam, detected $^3\vec{\mathrm{He}}(\vec{e}, e)$ elastic scattering and provided continuous high-precision monitoring of beam and target polarizations. The kinematic settings are listed in Table I.

TABLE I. Kinematic settings for quasielastic and elastic measurements.

Q^2 [(GeV/c)^2]	E (GeV)	E' (GeV)	θ (deg)
Electron arm (quasielastic)			
0.1	0.778	0.717	24.44
0.193	0.778	0.667	35.50
0.3	1.727	1.559	19.21
0.4	1.727	1.506	22.62
0.5	1.727	1.453	25.80
0.6	1.727	1.399	28.85
Hadron arm (elastic)			
0.1	0.778	0.760	23.73
0.2	1.727	1.691	15.04

B. Polarized electron source and beam line

The electron beam originated from a laser-driven "strained" GaAs source [47,48]. Polarized electrons were produced by illuminating a GaAs crystal in ultra-high vacuum with high-intensity circularly polarized laser light and removing electrons excited within the crystal by a strong external electric field. The polarization of the laser light was controlled electronically with the help of a Pockels cell. In this way, the electron beam helicity could be reversed rapidly (typically at 30 Hz), minimizing systematic errors in the measurement of spin-dependent asymmetries. To reduce systematic errors further, the overall sign of the beam helicity was reversed periodically by inserting a half-wave plate into the injector laser light path.

The standard Hall A beam-line instrumentation and beam raster [49] were employed. The beam energy was determined with an accuracy of better than 0.1% for all kinematics.

C. Polarized ^{3}He target

The experiment employed an optically pumped polarized ^{3}He gas target [49] of the spin-exchange type [50]. The target cell of this system contained high-pressure ($\approx$10 atm) ^{3}He gas as well as admixtures of rubidium (to facilitate optical pumping) and nitrogen (to quench radiation trapping). While background from the rubidium was negligible, the nitrogen admixture contributed on the order of 10^{-2} to the total target number density, requiring a small dilution correction (see Sec. IV C).

The target cell proper was a 40 cm long aluminum-silicate glass cell ($\rho = 2.76\,\mathrm{g/cm^3}$) with $\approx$1.2 mm thick walls and $\approx$135 μm thick end windows. A second target cell, the so-called reference cell, was available for calibration measurements. The reference cell had essentially the same dimensions as the target cell, except that it had no thin end windows but rather a uniform glass thickness throughout. Further details can be found in Refs. [51,52].

A typical ^{3}He nuclear polarization of 40% was achieved. The target spin direction was either $-62.5^\circ \pm 0.5^\circ$ or $-243.6^\circ \pm 0.5^\circ$ in the laboratory. (The difference of the two angles was not exactly 180° because of a calibration inaccuracy.) The target spin was reversed regularly throughout the experiment to reduce systematic errors from false asymmetries.

D. Spectrometers

The two spectrometers were equipped with their standard detector packages [49] consisting of a pair of vertical drift chambers (VDCs) for tracking, two segmented scintillator planes to generate the trigger and provide time-of-flight information, and a CO_2 gas Cherenkov detector for electron/pion separation. The HRSs had a usable momentum acceptance of approximately 9%. For further pion rejection, a preshower and a total-absorption shower counter were employed in the electron-arm HRS, while the hadron-arm HRS was instrumented with two thin lead-glass shower counters. The geometric solid angle of each HRS was limited to 6.0 msr by a rectangular tungsten collimator. The central scattering angle was surveyed to better than 0.1 mrad.

Trajectories of scattered particles were reconstructed using the VDC data and the standard optics model of the HRS [49]. The achieved momentum and scattering angle resolutions σ were better than 0.05% and 2 mrad, respectively. The transverse (i.e., along the beam) position resolution at the target was approximately 2 mm.

The pion rejection factor with the Cherenkov detectors alone was of order 100. Combining the Cherenkov and shower counters, a factor of over 1000 was achieved. Pion rejection was only a concern with the left-arm HRS, where pion production was not kinematically suppressed.

IV. ANALYSIS

A. Overview

The experimental raw asymmetry was calculated as

$$A^{\mathrm{exp}} = \frac{N_+ - N_-}{N_+ + N_-}, \tag{5}$$

where N_+ and N_- are the electron yields normalized by charge and electronic live time for positive and negative electron helicities, respectively.

To extract the physics asymmetry, corrections had to be made for dilution, background, radiative effects, and bin centering. Sources of dilution were the finite beam and target polarizations and scattering from the target walls and from the nitrogen gas in the target. Polarized background arose from the elastic radiative tail, which extended into the quasielastic region. Radiative corrections had to be applied to the raw quasielastic asymmetry. Bin centering corrections account for finite experimental acceptances.

The normalized yields in Eq. (5) can be written as

$$N = N^{\mathrm{qe}} + N^{\mathrm{ert}} + N^{\mathrm{emp}} + N^{N_2}, \tag{6}$$

where N^{qe}, N^{ert}, N^{emp}, and N^{N_2} are the contributions of quasielastic scattering from ^{3}He (before radiative and bin centering corrections), the elastic radiative tail, the target wall ("empty target") scattering, and scattering from nitrogen in the target cell, respectively. Using Eq. (6), one can define dilution factors for each of the three background contributions,

$$R^{\rm emp} = \frac{N^{\rm emp}}{N^{\rm qe} + N^{\rm ert}}, \tag{7}$$

$$R^{N_2} = \frac{N^{N_2}}{N^{\rm qe} + N^{\rm ert}}, \tag{8}$$

$$R^{\rm ert} = \frac{N^{\rm ert}}{N^{\rm qe}}, \tag{9}$$

and express the physics asymmetry as

$$A^{\rm phys} = (1 + R^{\rm ert})(1 + R^{\rm emp} + R^{N_2})\frac{A^{\rm exp}}{P_b P_t} - R^{\rm ert}A^{\rm ert} + \Delta A^{\rm qe} + \Delta A^{\rm bin}, \tag{10}$$

where $P_b P_t$ is the product of beam and target polarizations, $A^{\rm ert}$ is the asymmetry of the elastic radiative tail, $\Delta A^{\rm qe}$ is the radiative correction to the quasielastic asymmetry, and $\Delta A^{\rm bin}$, the bin centering correction. In Eq. (10), it is assumed that both the empty target and the N_2 contributions have no asymmetry. During the analysis, the empty target and N_2 false asymmetries were verified to be indeed consistent with zero.

Among the various factors in Eq. (10), $A^{\rm exp}$, $R^{\rm emp}$, and R^{N_2} could be determined directly from data, while $R^{\rm ert}$, $A^{\rm ert}$, $\Delta A^{\rm qe}$, and $\Delta A^{\rm bin}$ had to be determined from calculations or simulations. $P_b P_t$ was monitored continuously during the experiment via elastic polarimetry and was determined as the ratio between the measured elastic asymmetry and the simulated elastic asymmetry, as described in Sec. IV E.

B. Raw asymmetries

Raw asymmetries for both spectrometers were calculated according to Eq. (5). The quasielastic data were analyzed in terms of electron energy loss, $\omega = E - E'$, and grouped in bins of 10, 20, or 18.75 MeV width, depending on Q^2. The elastic data from the right-arm spectrometer were analyzed in terms of excitation energy, defined as

$$E_x = \sqrt{M^2 + 2M(E - E') - 4EE'\sin^2(\theta/2)} - M, \tag{11}$$

where M is the mass of the ^{3}He nucleus and θ the measured electron scattering angle. The raw elastic asymmetry was obtained from the region $-1 \leqslant E_x \leqslant +1$ MeV.

The angle between momentum transfer and target spin, θ^* in Eq. (1), varied between 0.2° and 10.0° depending on Q^2. This resulted in an $R_{TL'}$ contribution to the experimental asymmetry of less than 2%, as estimated by a PWIA calculation. The $R_{TL'}$ contribution was included in the theoretical calculations used to extract G_M^n. Even though theoretical predictions of $R_{TL'}$ are less accurate than those of $R_{T'}$ (because of the uncertainty in G_E^n), the uncertainty in our extracted G_M^n due to $R_{TL'}$ is negligible.

Raw asymmetries obtained for the four different combinations of target spin orientation and overall beam helicity sign were compared to check for false asymmetries. No statistically significant false signal was found. For the main physics analysis, data from the four polarization configurations were combined to minimize the statistical uncertainty.

C. Empty target and nitrogen dilution factors

Because the target cell was sealed, background from the target cell wall could not be measured directly by emptying the target. In addition, the background rate from the nitrogen buffer gas in the target could not be easily calculated because the nitrogen partial pressure could only be determined approximately when the cell was filled. Therefore, it was necessary to determine both background yields in separate calibration runs with the reference cell.

For each kinematics, quasielastic data were taken with the reference cell empty and filled with N_2 at several pressure values. The reference cell nitrogen yield as a function of nitrogen pressure was determined by subtracting the empty cell yield from the raw yields of the nitrogen runs. As the reference cell had physical dimensions very similar to those of the target cell, the reference cell nitrogen spectra could be used as a direct measure of the target cell nitrogen yield N^{N_2} provided that they were scaled to the nitrogen pressure inside the target cell.

The nitrogen partial pressure in the ^{3}He target cell was determined as follows: As shown in Fig. 3, the elastic nitrogen peak was clearly resolved in both the reference cell nitrogen spectrum (upper panel) and the spectrum from the ^{3}He target cell (lower panel), as measured with the right-arm spectrometer. Because the nitrogen pressure corresponding to the reference cell spectrum was known, the nitrogen pressure in the target cell could be determined by simple scaling. This procedure was only required for one kinematic setting since the nitrogen pressure was essentially constant throughout the experiment. The result was $p_{N_2} = 15.15 \pm 0.35$ kPa. The variation of the N_2 yield as a function of time was found to be within ±3%. We assigned an overall uncertainty of 5% to the measured nitrogen background yields.

Obtaining the empty target yield (i.e., the yield due to scattering from the ^{3}He target cell walls) from the empty reference cell data was complicated by two factors: (1) the background yield from the cell walls was a function of beam position and the beam tune, and thus reference cell runs did not necessarily reflect the exact background conditions present during production data taking, and (2) the reference cell glass wall thickness and density were not equal to those of the target cell.

Regarding factor (1), the variation of the empty target yields obtained under nominally identical experimental conditions but at different points in time were compared and found to agree within ±15%.

Regarding factor (2), we note that (a) the target and reference cells were made of different types of glass, and the target cell glass density was about 9% larger than that of the reference cell, (b) the thickness of the reference cell side walls was found to be, on average, 2.5% thinner than that of the target cell, as determined by laser interferometry [53], and (c) the target cell had very thin (135μm) end windows, while the corresponding reference cell end windows were about as thick (1.2 mm) as its side walls. Contributions from the end windows were almost completely eliminated by using a vertex position cut. The thicker end windows of the reference cell therefore mattered only insofar as they gave rise to small non-Gaussian tails that extended into the acceptance. These tails were largely

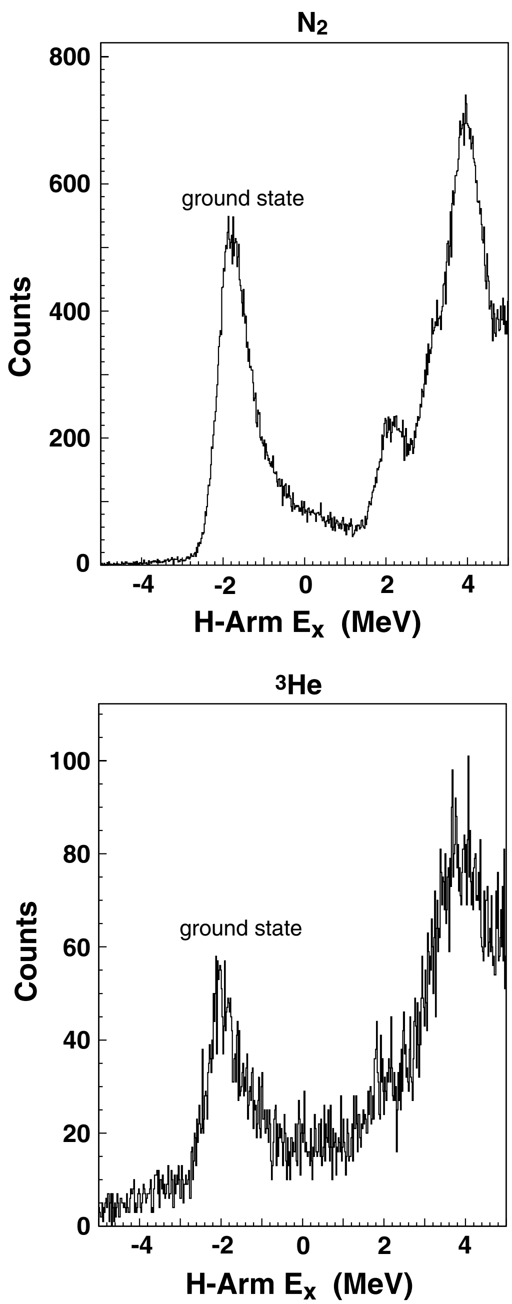

FIG. 3. Raw yields measured with the right-arm spectrometer in the region of the N_2 elastic peak using the N_2 reference cell (upper panel) and the ^{3}He target (lower panel) as a function of excitation energy E_x. The leftmost peak represents the N_2 ground state; other peaks are related to excited states of N_2.

due to event reconstruction errors. They were estimated to contribute on the order of a few percent to the total reference cell yield; this was comparable in magnitude to the correction necessary for the thinner and less dense glass walls of the reference cell. Since these corrections were small and difficult to compute accurately and could be expected to partly cancel each other, they were ignored in the analysis, and the resulting error of a few percent was included in the overall systematic

TABLE II. Estimated systematic uncertainties of the quasielastic $A_{T'}$ asymmetry measurements. HC denotes helicity correlated. The two columns of uncertainties correspond to the quasielastic measurements at lower Q^2 (0.1 and 0.2) and higher Q^2 (0.3–0.6). Values in the center of both columns are common to all kinematics.

Source	$\delta A_{T'}/A_{T'}(\%)$	
	$Q^2 \leqslant 0.2$	$Q^2 \geqslant 0.3$
$P_b P_t$	1.3	1.7
Empty target subtraction	1.0	0.25
N_2 background subtraction	0.3	
QE radiative correction	0.3	
Elastic radiative tail	0.3	
Spectrometer acceptance	0.5	
HC scintillator efficiency	0.1	
HC wire chamber efficiency	0.1	
HC computer dead time	0.1	
HC beam current shift	0.1	
HC beam motion	0.1	
Pion contamination	0.1	
Total	1.8	1.9

uncertainty of the empty target dilution factor. The empty cell background yield of the ^{3}He target was taken to be identical to that of the empty reference cell, and an overall systematic uncertainty of 25% was assigned to the empty yield, taking into consideration the statistical uncertainty, the time variation of the yield due to beam-tune variations, and the differences in the cell properties.

The empty target cell and the N_2 dilution factors (R^{emp} and R^{N_2}) were determined by combining all empty target and nitrogen runs, respectively, at the same kinematics. The nominator in Eqs. (7) and (8) was calculated according to Eq. (6) as $N^{\mathrm{qe}} + N^{\mathrm{ert}} = N - N^{\mathrm{emp}} - N^{N_2}$. The time variation of the yields was included in the systematic uncertainty of each contribution. The uncertainties are given in Table II.

An ad hoc upward correction of all the empty target dilution factors by a factor of 2, which was used in our prior publications [17,23,53], was dropped in this analysis, as it had been motivated by an unphysical tail of apparently poorly reconstructed events seen in the right-arm spectrometer. Instead, a more conservative uncertainty was assigned to the empty target background subtraction at $Q^2 = 0.1$ and $0.2\,(\mathrm{GeV}/c)^2$, where the empty target background is largest.

D. Monte Carlo simulation

A full Monte Carlo simulation was developed for this experiment [24], which allowed the averaging of theoretical results over the experimental acceptances and accounted for multiple scattering, ionization energy loss, external bremsstrahlung, and internal radiative corrections.

To calculate the spin-dependent elastic and quasielastic radiative tails, internal radiation effects were modeled using the covariant formalism developed in Ref. [54], generalized to the case of low-Q^2 quasielastic scattering. This formalism accommodates polarization degrees of freedom. Standard, unpolarized radiative corrections [55] were applied to the elastic peak region.

E. Elastic polarimetry

The beam and target polarizations, P_b and P_t, were monitored continuously during the experiment using elastic polarimetry. Because the ^{3}He elastic form factors, the charge form factor F_c and the magnetic form factor F_m, are known very well experimentally [56], the ^{3}He elastic asymmetry can be calculated as [32]

$$A_{\rm el} = \frac{-2\tau v_{T'}\cos\theta^*\mu_A^2 F_m^2 + 2\sqrt{2\tau(1+\tau)}v_{TL'}\sin\theta^*\cos\phi^*\mu_A Z F_m F_c}{(1+\tau)v_L Z^2 F_c^2 + 2\tau v_T \mu_A^2 F_m^2}. \tag{12}$$

Here, the v_i are kinematic factors, $\tau = Q^2/4M^2_{^3\rm He}$, and $\mu_A = \mu_{^3\rm He}(M_{^3\rm He}/M_N) = -6.37$, where M_N is the nucleon mass. To allow direct comparison with data, the Monte Carlo program described in Sec. IV D was used to average Eq. (12) over the experimental acceptance. We then obtained

$$P_b P_t = \frac{A_{\rm el}^{\rm exp}}{A_{\rm el}^{\rm sim}} \times f_{N_2} f_{\rm emp}, \tag{13}$$

where $A_{\rm el}^{\rm exp}$ and $A_{\rm el}^{\rm sim}$ are the measured and simulated elastic asymmetry, respectively, and f_{N_2} and $f_{\rm emp}$ are correction factors for the measured nitrogen and empty target cell dilution, respectively, for the elastic data sets.

The data for $A_{\rm el}^{\rm exp}$ are listed in Table III. Separate data are shown for each of the four possible spin and helicity configurations, which are largely consistent within their errors. For the evaluation of Eq. (13), the weighted average of the data for the four spin combinations was used. The dilution factors f_{N_2} and $f_{\rm emp}$ were obtained using the procedure described in Sec. IV C.

No radiative corrections were applied to the elastic data, since most radiative effects were included in the simulation. Missing is the spin dependence of the Schwinger correction, which we deemed negligible.

At the two beam energies, $E = 0.778$ and $E = 1.727$ GeV, the overall relative systematic uncertainty in $P_b P_t$ was 1.3% and 1.7%, respectively. In each case, the dominant contribution came from the uncertainty in the form factors F_c and F_m, followed by the contribution from the uncertainty in the target spin direction.

The average $P_b P_t$ so obtained was $0.208 \pm 0.001 \pm 0.004$, where the errors are statistical and systematic, respectively. As a cross-check, independent measurements of the polarizations were obtained using Møller beam polarimetry and NMR target polarimetry, yielding an overall average value of $P_b P_t = 0.215 \pm 0.013$ [57]. The elastic polarimetry results were used for further analysis and averaged for each quasielastic kinematic setting separately (cf. Table III) to account for possible slow changes of the polarizations with time. The observed stability of the polarization data suggests that this procedure was adequate.

TABLE III. Measured elastic asymmetries $|A_{\rm el}^{\rm exp}|$ for the six quasielastic kinematic settings. $Q^2_{\rm qe}$ and $Q^2_{\rm el}$ are the momentum transfers of the quasielastic and elastic measurements, respectively. The four columns of results correspond to the four combinations of the signs of the target spin and beam helicity. Column headings indicate the laboratory target spin angle and position of the accelerator injector half-wave plate. Uncertainties are statistical.

$Q^2_{\rm qe}$ [(GeV/c)^2]	$Q^2_{\rm el}$ [(GeV/c)^2]	$\|A_{\rm el}^{\rm exp}(\%)\|$			
		−62.5°/in	−62.5°/out	−243.6°/in	−243.6°/out
0.1	0.1	1.333 ± 0.027	1.043 ± 0.027	1.067 ± 0.02	1.208 ± 0.030
0.193	0.1	1.078 ± 0.037	1.177 ± 0.027	1.190 ± 0.021	1.102 ± 0.023
0.3	0.2	1.251 ± 0.096	1.222 ± 0.048	1.107 ± 0.067	1.206 ± 0.075
0.4	0.2	1.181 ± 0.055	1.314 ± 0.061	1.168 ± 0.06	1.258 ± 0.057
0.5	0.2	1.265 ± 0.042	1.307 ± 0.039	1.200 ± 0.045	1.184 ± 0.041
0.6	0.2	1.258 ± 0.049	1.301 ± 0.047	1.110 ± 0.05	1.096 ± 0.05

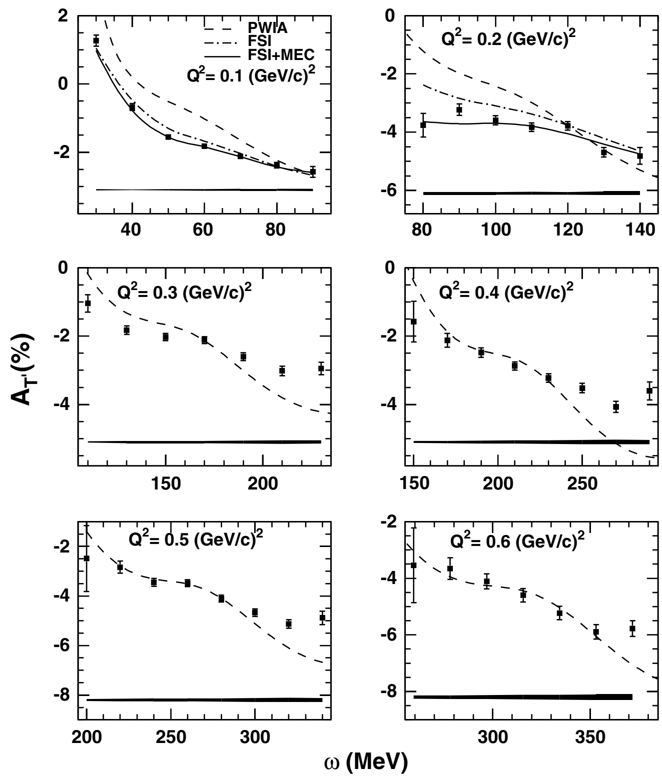

FIG. 4. Quasielastic $A_{T'}$ asymmetry results vs energy transfer ω. Errors on data points are statistical. The systematic uncertainty is shown as an error band at the bottom of each panel.

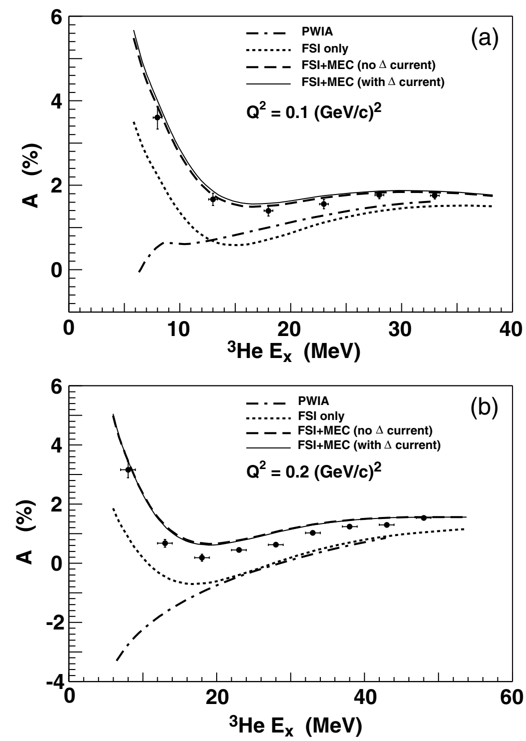

FIG. 5. Experimental asymmetry in the region of the ^{3}He breakup threshold together with theoretical calculations for (a) $Q^2 = 0.1\,(\mathrm{GeV}/c)^2$ and (b) $Q^2 = 0.2\,(\mathrm{GeV}/c)^2$. The calculations differ only in the description of the reaction mechanism.

V. ASYMMETRY RESULTS

A. Quasi-elastic transverse asymmetry $A_{T'}$

Results for the quasielastic transverse asymmetry $A_{T'}$ at the six measured Q^2 points are shown in Fig. 4. Numerical values can be found in Ref. [53]. The errors on the data are statistical only, while the systematic uncertainty is shown as an error band at the bottom of each panel. A detailed breakdown of the systematic uncertainties is presented in Table II. The experimental data were corrected for radiative effects, background, and dilution, as described in detail in the previous section.

Also shown in Fig. 4 are the results of several calculations. Dashed lines represent the PWIA calculation [33]. The dash-dotted and solid curves at the two kinematics with the lowest Q^2 represent, respectively, Faddeev results with inclusion of FSI only [15] and with inclusion of both FSI and MEC corrections [16]. The calculation from Ref. [16] will be referred to as the "full Faddeev calculation" in the following. All theory results were averaged over the spectrometer acceptances using the Monte Carlo simulation described in Sec. IV D. Further details on the calculations are given in Sec. II.

One observes excellent agreement of the data with the full Faddeev calculation over the entire ω range at $Q^2 = 0.1$ and $0.2\,(\mathrm{GeV}/c)^2$, while PWIA describes the data well at the higher Q^2, particularly in the region around the quasielastic peak (near the center of the ω range in each panel).

B. Asymmetry in the threshold region

The asymmetries measured in the region around the two- and three-body breakup thresholds (5.5 and 7.7 MeV, respectively) are shown in Fig. 5. These results provide a sensitive test of the quality of the Faddeev calculations.

The threshold asymmetry data were taken with the hadron-arm spectrometer as a byproduct of the elastic polarimetry and were analyzed in the same manner as the quasielastic asymmetries. The kinematics are given in the lower part of Table I. The Q^2 values of 0.1 and 0.2 $(\mathrm{GeV}/c)^2$ in Fig. 5 correspond to the momentum transfer at the elastic peak. The data are plotted as a function of the excitation energy E_x, defined in Eq. (11). Horizontal errors represent the uncertainty in determining E_x, which was dominated by the uncertainty in the beam energy. The vertical errors are the statistical and systematic errors added in quadrature. Tables of the data and uncertainties can be found in Ref. [58].

Figure 5 also shows various theoretical results. Dot-dashed lines depict those of the PWIA calculations [33], while those of Faddeev calculations with FSI only [15] appear as dotted lines. The full Faddeev calculation [16], which includes both FSI and MEC but not the Δ-isobar current, is represented by dashed lines. The solid lines were obtained with the full calculation after including Δ-isobar currents. These calculations employed the AV18 NN interaction potential. Results obtained with the BonnB potential were found to be only slightly different from the AV18 results and in even better agreement with the data [24].

As can be seen, the agreement between PWIA calculations and the data is poor at both kinematics, which confirms the expectation that FSI and MEC corrections are essential in this region. Indeed, the inclusion of FSI improves the agreement significantly, and good agreement is achieved once MECs are added. It has been shown that substantial MECs are needed to describe the measured elastic electromagnetic form factors of three-nucleon systems [59]. The corresponding physics should extend into the low-ω region of inelastic scattering as well.

The good agreement between the full calculation and the data at $Q^2 = 0.1\,(\mathrm{GeV}/c)^2$ suggests that FSI and MEC effects are properly treated in the full calculation. The insensitivity of the results to the addition of Δ-isobar currents implies a weak model dependence of the MEC corrections. The small, systematic discrepancy at $Q^2 = 0.2\,(\mathrm{GeV}/c)^2$ may indicate that some Q^2 dependent effects, such as relativistic and three-nucleon force effects, become important already at this momentum transfer.

VI. EXTRACTION OF THE NEUTRON MAGNETIC FORM FACTOR

The neutron magnetic form factor G_M^n can be extracted from the measured ^{3}He quasielastic transverse asymmetry $A_{T'}$ if a calculation is available that predicts $A_{T'}$ as a function of G_M^n. If we assume, following Eq. (4), that the asymmetry is a function of $(G_M^n)^2$, we can expand $A_{T'}$ around a reference G_M^n value, G_0, such that

$$A_{T'}\left({G_M^n}^2\right) = A_{T'}\left(G_0^2\right) + \frac{\partial A_{T'}}{\partial\left({G_M^n}^2\right)}\left(G_0^2\right)\left({G_M^n}^2 - G_0^2\right) + O\left(\left({G_M^n}^2 - G_0^2\right)^2\right). \quad (14)$$

For ease of notation, we normalize all G_M^n values to a convenient reference scale (the Höhler parametrization [39] in this case) so that $G_0 = 1$. Equation (14) can be solved for G_M^n, assuming the second-order term is small:

$$G_M^n = \sqrt{1 + \frac{A_{T'}\left({G_M^n}^2\right) - A_{T'}(1)}{\partial A_{T'}/\partial\left({G_M^n}^2\right)(1)}}. \quad (15)$$

Here, $A_{T'}({G_M^n}^2)$ is the measured asymmetry. The predicted asymmetry, $A_{T'}(1)$, and the sensitivity factor, $\partial A_{T'}/\partial({G_M^n}^2)(1)$, are the output of the model calculation. The latter two parameters were determined using the full Faddeev calculation [16] for the lowest two Q^2 points of this experiment, and the PWIA calculation [33] for the remaining four Q^2. Results were averaged over the experimental acceptance using the Monte Carlo program described in Sec. IV D. At each kinematical point, asymmetries were generated for several ω-bins around the quasielastic peak. Within each bin, G_M^n was varied around the reference value G_0 by adding a constant to the functional form $G_M^n(Q^2)$ given by the Höhler model.

$G_M^n(Q^2)$ was extracted for each ω bin via Eq. (15). A different functional form, a general second-order expansion of $A_{T'}(G_M^n)$, was also tried. The differences between the form factors extracted via these two methods was found to be negligible (<0.1%) for all kinematics [53].

The final G_M^n results were obtained by taking the weighted average of the G_M^n values from the ω bins closest to the quasielastic peak. The ω region used for the extraction of G_M^n covered a width of 30 MeV at $Q^2 = 0.1$ and 0.2, 60 MeV at $Q^2 = 0.3$, 40 MeV at $Q^2 = 0.4$ and 0.5, and 56.25 MeV at $Q^2 = 0.6\,(\mathrm{GeV}/c)^2$.

The extraction procedure gives rise to a systematic error due to the uncertainty in the experimental determination of the energy transfer ω (± 3 MeV). The uncertainty in ω results in an uncertainty as to the ω region over which to integrate the theoretical calculation used for the extraction of G_M^n. A shift of bin boundaries generally translates into a different average value of $A_{T'}$ for the bin and hence a different extracted G_M^n value.

Furthermore, as can be seen in Fig. 4, the theoretical calculations, especially PWIA, match the data best in the immediate vicinity of the quasielastic peak where corrections to the plane wave picture are smallest, whereas deviations may occur off the peak. This can introduce an artificial ω dependence into the extracted G_M^n which goes beyond the effect of the kinematic variation of Q^2 with ω. For this effect to be minimized, the bins used for the G_M^n extraction should be centered around the quasielastic peak, assuming that deviations are distributed roughly symmetrically. The experimental uncertainty in ω may cause improper centering, resulting in a bias in extracting G_M^n. The calculated uncertainties in G_M^n resulting from the uncertainty in ω can be found in Table IV.

VII. ESTIMATE OF THEORETICAL UNCERTAINTIES

A. Nucleon-nucleon potential and nucleon form factors

The effect of different NN potential models on the predicted asymmetry $A_{T'}$ was studied by carrying out the full Faddeev calculation with the Argonne AV18 and the Bonn B NN potentials at several representative kinematics. In a similar manner, to estimate the uncertainty due to the elastic nucleon form factors other than G_M^n, Faddeev calculations were performed in which these quantities were varied individually by their published experimental uncertainties. The resulting uncertainty in G_M^n from these sources, when combined in quadrature, is less than 1% for all kinematics (cf. Table V).

TABLE IV. Results for G_M^n as a ratio to the dipole form factor G_D and uncertainties obtained in the present experiment. The data have changed slightly from our previously published numbers [17,23] due to differences in the analysis.

Q^2 [(GeV/c)^2]	$G_M^n/(\mu_n G_D)$	$\delta G_M^n/G_M^n$			
		Stat. (%)	Syst. (%)	Model (%)	Total (%)
0.1	0.9481	1.36	1.08	2.2	2.8
0.193	0.9511	1.35	1.26	2.1	2.8
0.3	0.9577	1.35	1.86	5.3	5.8
0.4	0.9694	1.45	1.28	2.5	3.2
0.5	0.9689	1.35	1.25	2.1	2.8
0.6	0.9939	1.55	1.38	2.0	2.9

TABLE V. Estimated uncertainties of the extracted form factor G_M^n. Systematic uncertainties include contributions from the asymmetry measurement ($A_{T'}$; see Table II), the energy transfer determination (ω), and the other nucleon form factors (G_E^p, G_M^p, and G_E^n). Theoretical (model) uncertainties include contributions from the NN potential model, off-shell effects, FSI, MEC, three-body forces (3BF), Coulomb corrections, and relativistic effects. In the totals, the uncertainties have been added in quadrature, ignoring any possible correlations between the contributions, which may very well exist, especially for the model uncertainties. Thus, the numbers should be taken with appropriate caution.

Q^2 [(GeV/c)^2]	Systematic $\delta G_M^n/G_M^n$ (%)						Model $\delta G_M^n/G_M^n$(%)							
	$A_{T'}$	ω	G_E^p	G_M^p	G_E^n	Total	NN	Off-shell	FSI	MEC	3BF	Coulomb	Relativity	Total
0.1	0.90	0.3	0.44	0.21	0.14	1.08	0.45	1.6	0.5	1.0	0.6	1.0	0.5	2.2
0.193	0.90	0.6	0.53	0.35	0.13	1.26	0.40	1.2	0.5	1.0	1.0	1.0	0.7	2.1
0.3	0.95	1.4	0.56	0.52	0.17	1.86	0.50	0.5	4.5	1.8	1.2	1.0	0.5	5.3
0.4	0.95	0.45	0.46	0.56	0.08	1.28	0.45	0.5	1.8	1.2	1.2	1.0	0.5	2.5
0.5	0.95	0.15	0.38	0.60	0.38	1.25	0.40	0.5	0.7	0.5	1.4	1.0	0.5	2.1
0.6	0.95	0.10	0.32	0.64	0.69	1.38	0.40	0.5	0.5	0.5	1.4	1.0	0.5	2.0

B. Relativistic effects

Since the full Faddeev calculation is nonrelativistic, it was particularly important to estimate quantitatively the size of relativistic corrections. Such an estimate can be obtained within the PWIA, which is theoretically well understood. Standard PWIA calculations take most relativistic effects into account (cf. Sec. II B). It is straightforward to modify the relativistic parts of the PWIA formalism to reflect the nonrelativistic approximations made in the Faddeev formalism. The differences between the results of such a modified, nonrelativistic PWIA calculation and the standard relativistic PWIA results provide an estimate of the error in the Faddeev results due to relativistic effects.

To this end, we modified three parts of the standard PWIA formalism: (1) approximations were made to the relativistic kinematics, (2) the phase space and integral ranges of the Fermi momentum and the missing mass of the many-fold integration of the $^3\vec{\mathrm{He}}(\vec{e}, e')$ cross-section were changed according to the nonrelativistic kinematics, and (3) the relativistic hadronic current was translated into an approximate nonrelativistic form [60,61]. Among the three modifications, the change of the kinematics was found to dominate [62].

With the PWIA results at hand, we developed a heuristic "recipe" [62] to allow an approximate correction of the Faddeev results for relativistic effects. The recipe could be readily applied to existing Faddeev results without the need for recomputation.

Results of these studies are shown in Fig. 6. The three curves represent the original relativistic PWIA results (solid line), nonrelativistic PWIA results obtained using the modifications described above (dot-dashed line), and nonrelativistic PWIA results corrected for relativistic effects though the recipe (dashed line). As can be seen, the heuristic correction works well up to about $Q^2 = 0.4\,(\mathrm{GeV}/c)^2$.

The acceptance-averaged difference between the relativistic and nonrelativistic PWIA results at $Q^2 = 0.1$ and $0.2\,(\mathrm{GeV}/c)^2$ was taken as the model uncertainty of the Faddeev results due to relativity.

C. FSI and MEC

To estimate FSI contributions to $A_{T'}$, we carried out the Faddeev calculation up to $Q^2 = 0.4\,(\mathrm{GeV}/c)^2$ with the inclusion of FSI effects only. [Already at $Q^2 = 0.3\,(\mathrm{GeV}/c)^2$, the $3N$ center-of-mass energy is above the pion production threshold, and therefore the nonrelativistic framework is no

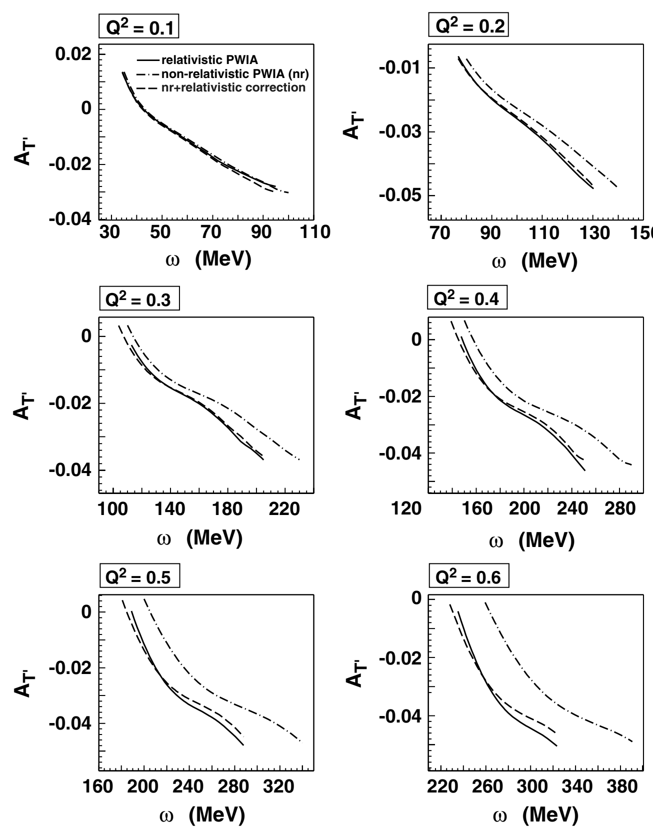

FIG. 6. Relativistic effects in $A_{T'}$. The solid line is the standard relativistic PWIA calculation [33]. The dot-dashed curve is the nonrelativistic PWIA calculation that we developed, and the dashed curve is the nonrelativistic PWIA calculation with heuristic relativistic corrections applied (see text).

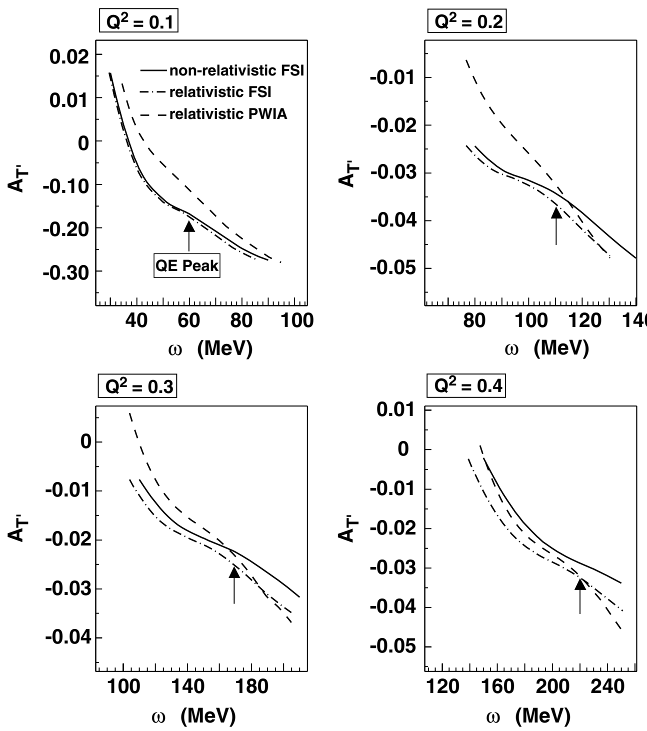

FIG. 7. FSI effect study. The dashed curve represents the standard (relativistic) PWIA calculation, the solid curve is the (nonrelativistic) Faddeev calculation with FSI effects only, and the dot-dashed curve depicts the same Faddeev calculation but with relativistic corrections applied. Comparing the dashed and dot-dashed curves, one can estimate the effect of FSI in $A_{T'}$.

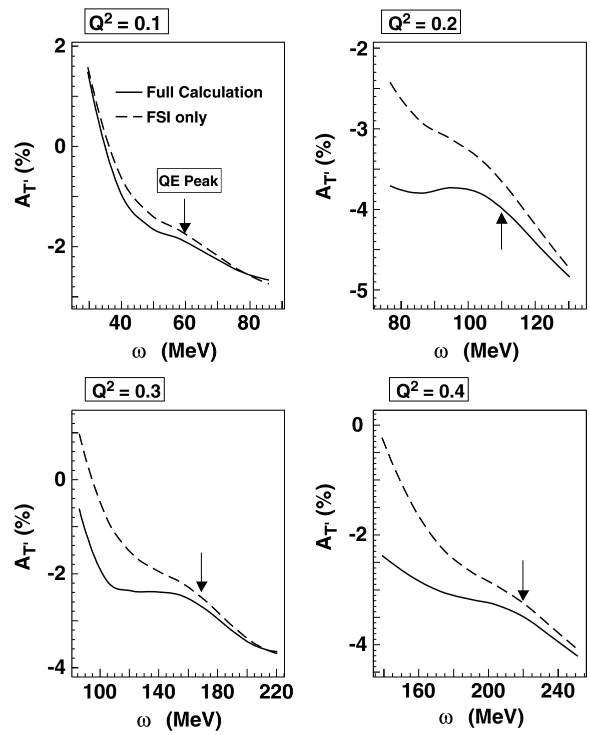

FIG. 8. MEC effect study. Comparing the full calculation (solid curve) with the calculation with FSI effects only (dashed curve), one can estimate contributions to $A_{T'}$ from MEC effects.

longer valid.] Next, we applied relativistic corrections to the Faddeev results using the ad hoc prescription developed in Sec. VII B. The "relativistic FSI" results so obtained were compared with the results of the standard (relativistic) PWIA calculation, as illustrated in Fig. 7. The difference between the two calculations in the region around the quasielastic peak is a measure of the FSI effects at each Q^2 point. For the two highest Q^2 values, we extrapolated the FSI data using a purely empirical fit to the lower Q^2 values, as shown in Fig. 9(a). As expected [27–29], FSI effects decrease significantly as Q^2 increases.

In a similar manner, we can estimate the size of MEC effects by comparing the Faddeev results with inclusion of FSI only, obtained in the FSI study above, to those of the full Faddeev calculation. Results are shown in Fig. 8, and differences between the two calculations are plotted as solid triangles in Fig. 9(b). As with FSI, we observe a sharp decrease of MEC corrections with increasing Q^2.

It is interesting to compare our results for the size of MEC corrections with those obtained from theoretical studies of quasielastic inclusive scattering from polarized deuterium, $^2\vec{\mathrm{H}}(\vec{e}, e')$ [30]. The deuterium results are shown in Fig. 9(b) as solid squares. As can be seen, the data are similar to those calculated for the corresponding ^{3}He reaction. Assuming a similar underlying physical mechanism, we use the MEC data from deuterium to estimate the size of MEC corrections to the $^3\vec{\mathrm{He}}(\vec{e}, e')$ data at the highest two Q^2 values of our data set.

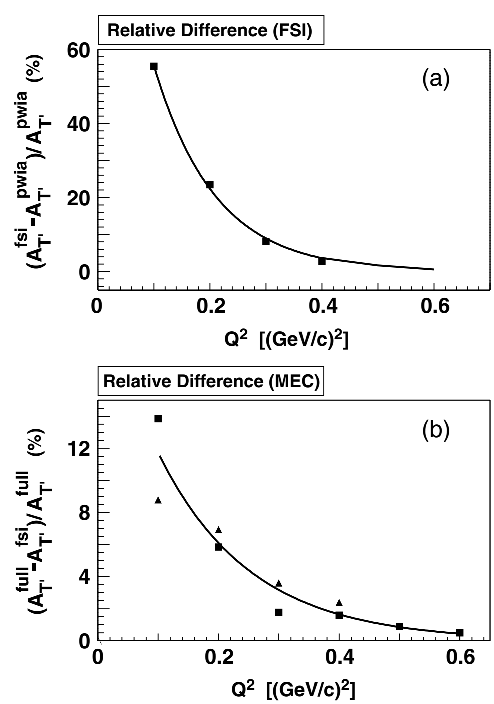

FIG. 9. Estimated magnitude of (a) FSI effects and (b) MEC effects in $A_{T'}$ as a function of Q^2. In (b), the solid triangles represent results obtained in our study of $^3\vec{\mathrm{He}}(\vec{e}, e')$, while the solid squares depict predictions from a calculation of $^2\vec{\mathrm{H}}(\vec{e}, e')$ in Ref. [30]. Curves are empirical fits to the data.

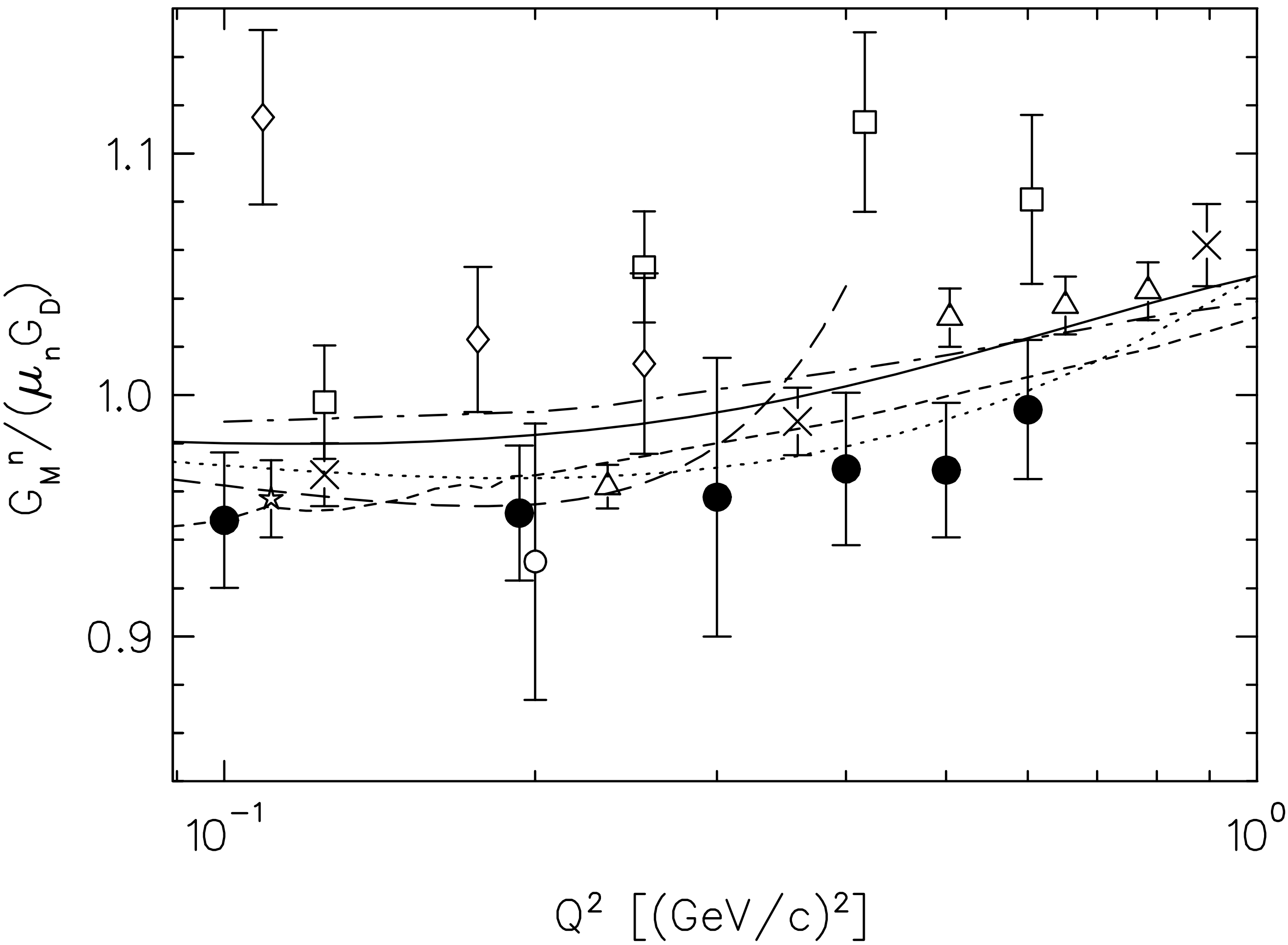

FIG. 10. World G_M^n data since 1990. Data points represent the results of the Bonn [7,8] (□), MIT-Bates [6,20] (◇, ○), NIKHEF/PSI [9] (☆), and the Mainz/PSI [10,11] (△, ×) experiments as well as those of the present measurement (●), where the error bars are the total uncertainties reported. Also shown are the results of various model calculations: Hammer and Meißner [65] (solid curve), Holzwarth [66] (dotted), Kubis and Meißner [67] (long-dashed), Lomon [68] (dashed-dotted), and de Melo *et al*. [69] (short-dashed).

These studies provide rough estimates of the expected magnitudes of the respective effects. They are not reliable enough to be used to correct the PWIA results for FSI and MEC contributions. Consequently, we use the numbers obtained above as estimates of the model uncertainties inherent in the PWIA. We take the numbers as the 1σ values of the uncertainties, which we assume to be symmetric. The resulting model uncertainties in G_M^n are detailed in Table V and are propagated into the final G_M^n errors given in Table IV.

D. Off-shell effects

Off-shell corrections to the single nucleon current, including the part of the current that describes polarization degrees of freedom [63], are purely relativistic in nature. While the PWIA calculation used here includes off-shell effects, they are ignored in the Faddeev calculation.

We estimated the magnitude of required off-shell corrections to the Faddeev results by comparing results of a modified version of the PWIA formalism that treats nucleons as on-shell [62] to those of the standard PWIA.

In addition, theoretical uncertainties due to different possible off-shell prescriptions were estimated using the difference of PWIA results obtained with the deForest CC1 and CC2 forms [64]. (The standard PWIA calculation employs CC1.) While this number represents a minimum uncertainty, as various other off-shell prescriptions are equally permissible [63], PWIA calculations using the CC1 form have been found to agree better with experimental data of unpolarized ^{3}He(e, e') scattering than those using other prescriptions [33]. This suggests the use of the CC1 prescription as a reference in the polarized case as well.

Results are given in Table V. Interestingly, off-shell effects dominate the model uncertainty in G_M^n at the lowest two Q^2 values.

VIII. FORM FACTOR RESULTS AND DISCUSSION

Numerical values for G_M^n extracted in this work are given in Table V [in units of the empirical dipole parametrization, $G_D = (1 + Q^2/0.71)^{-2}$] and shown in Fig. 10 along with the existing world data set published since 1990 [6–11,20]. The error bars represent the total uncertainties reported by the respective experiments, including model uncertainties.

The results appear to be largely consistent, with the exception of the early ^{2}H$(e, e'n)$ data from Bates [6] and the first ^{2}H$(e, e'n)/^2$H$(e, e'p)$ ratio measurement from Bonn [7,8]. The discrepancy of the data of these two experiments with the rest of the world data has been attributed to incomplete corrections for neutrons that miss the neutron detector [12]. The data of the Bonn experiment [7] were reanalyzed subsequently [8], resulting in a downward correction of the G_M^n data. Figure 10 shows the reanalyzed data. We note the satisfactory agreement between the more recent, high-precision deuterium ratio measurements [9–11] and the data from this work. The agreement is well within the total uncertainties of the experiments, except at $Q^2 = 0.5$ and $0.6\,(\mathrm{GeV}/c)^2$, where the ^{3}He results are low by about 5%.

Also shown in Fig. 10 are several theoretical results: a recent dispersion-theoretical fit by Hammer and Meißner [65] (solid curve), a chiral soliton model by Holzwarth [66] (dotted curve), a relativistic baryon chiral perturbation theory (ChPT) calculation by Kubis and Meißner [67] (long-dashed curve), a vector meson dominance (VMD) fit by Lomon [68] (dashed-dotted curve), and a recent light-front quark model by de Melo *et al*. [69] (short-dashed curve). It should be noted that all of these models contain one or more free parameters that have been fitted to existing data.

As can be seen, the dispersion-theoretical fit [65] and the VMD fit [68] agree best with the data at $Q^2 > 0.3\,(\mathrm{GeV}/c)^2$, while the ChPT results [67] and the chiral soliton model [66] match the data better at lower Q^2. The ChPT model is expected to be good only up to $Q^2 \approx 0.3\,(\mathrm{GeV}/c)^2$, but it clearly works very well in its region of validity. The light-front model of de Melo *et al*. [69] arguably shows the best overall agreement. The models by Holzwarth [66], Lomon [68], and de Melo *et al*. [69] also describe well the proton form factor ratio G_E^p/G_M^p and other elastic nucleon form factors in this Q^2 region.

IX. CONCLUSIONS

In conclusion, we have determined the neutron magnetic form factor G_M^n from quasielastic $^3\vec{\mathrm{He}}(\vec{e}, e')$ data. At Q^2 of 0.1 and $0.2\,(\mathrm{GeV}/c)^2$, we used a state-of-the-art Faddeev calculation that includes FSI and MEC effects and a PWIA at four additional points between $Q^2 = 0.3$ and $0.6\,(\mathrm{GeV}/c)^2$. The results agree within the total uncertainties with those obtained by several recent measurements on deuterium, except at $Q^2 = 0.5$ and $0.6\,(\mathrm{GeV}/c)^2$ where the ^{3}He results are slightly low. A consistent picture of the behavior of G_M^n in this Q^2 region is beginning to emerge, although further precision measurements as well as improved model calculations, such as the extension of the Faddeev formalism to higher Q^2 in the case of polarized ^{3}He, remain highly desirable.

In addition, we have measured $A_{T'}$ in the two- and three-body breakup threshold region at Q^2 of 0.1 and $0.2\,(\mathrm{GeV}/c)^2$ where the sensitivity to FSI and MEC effects is particularly high. The results agree well with the predictions of the Faddeev model, especially at $Q^2 = 0.1\,(\mathrm{GeV}/c)^2$, confirming the validity of the treatment of FSI and MEC effects in this formalism.

ACKNOWLEDGMENTS

We thank the Hall A technical staff and the Jefferson Lab Accelerator Division for their outstanding support during this experiment. We also thank T. W. Donnelly for many helpful discussions. This work was supported in part by the U.S. Department of Energy, DOE/EPSCoR, the U.S. National Science Foundation, the Science and Technology Cooperation Germany-Poland, and the Polish Committee for Scientific Research under Grant No. 2P03B00825, the Ministero dell'Università e della Ricerca Scientifica e Tecnologica (Murst), the French Commissariat à l'Énergie Atomique, Centre National de la Recherche Scientifique (CNRS), Conseil Régional d'Auvergne, the Italian Istituto Nazionale di Fisica Nucleare (INFN), a grant of the European Foundation Project INTAS-99-0125, and by DOE Contract DE-AC05-84ER40150, Modification No. M175, under which the Southeastern Universities Research Association (SURA) operates the Thomas Jefferson National Accelerator Facility. The numerical calculations were performed on the PVP machines at the U.S. National Energy Research Scientific Computer Center (NERSC) and the CRAY SV1 of the NIC in Jülich.

[1] H. Gao, Int. J. Mod. Phys. E **12**, 1 (2003); **12**, 567(E) (2003).
[2] D. H. Beck and R. D. McKeown, Annu. Rev. Nucl. Sci. **51**, 189 (2001).
[3] K. S. Kumar and P. A. Souder, Prog. Part. Nucl. Phys. **45**, S333 (2000).
[4] M. Jones *et al*., Phys. Rev. Lett. **84**, 1398 (2000).
[5] O. Gayou *et al*., Phys. Rev. Lett. **88**, 092301 (2002).
[6] P. Markowitz *et al*., Phys. Rev. C **48**, R5 (1993); final results in P. Markowitz, Ph.D. thesis, College of William and Mary, 1992.
[7] E. E. W. Bruins *et al*., Phys. Rev. Lett. **75**, 21 (1995).
[8] B. Schoch (private communication).
[9] H. Anklin *et al*., Phys. Lett. **B336**, 313 (1994).
[10] H. Anklin *et al*., Phys. Lett. **B428**, 248 (1998).
[11] G. Kubon *et al*., Phys. Lett. **B524**, 26 (2002).
[12] J. Jourdan, I. Sick, and J. Zhao, Phys. Rev. Lett. **79**, 5186 (1997); E. E. W. Bruins *et al*., *ibid*. **79**, 5187 (1997).
[13] B. Blankleider and R. M. Woloshyn, Phys. Rev. C **29**, 538 (1984).
[14] L. D. Faddeev, Zh. Eksp. Teor. Fiz. **39**, 1459 (1960) [Sov. Phys. JETP **12**, 1014 (1961)].
[15] J. Golak, H. Kamada, H. Witała, W. Glöckle, and S. Ishikawa, Phys. Rev. C **51**, 1638 (1995); V. V. Kotlyer, H. Kamada, W. Glöckle, and J. Golak, Few-Body Syst. **28**, 35 (2000).
[16] J. Golak, G. Ziemer, H. Kamada, H. Witała, and W. Glöckle, Phys. Rev. C **63**, 034006 (2001).
[17] W. Xu *et al*., Phys. Rev. Lett. **85**, 2900 (2000).
[18] C. E. Jones *et al*., Phys. Rev. C **47**, 110 (1993).
[19] A. K. Thompson *et al*., Phys. Rev. Lett. **68**, 2901 (1992).

[20] H. Gao *et al.*, Phys. Rev. C **50**, R546 (1994); H. Gao, Nucl. Phys. **A631**, 170c (1998).
[21] J.-O. Hansen *et al.*, Phys. Rev. Lett. **74**, 654 (1995).
[22] M. Meyerhoff *et al.*, Phys. Lett. **B327**, 201 (1994).
[23] W. Xu *et al.*, Phys. Rev. C **67**, 012201(R) (2003).
[24] F. Xiong *et al.*, Phys. Rev. Lett. **87**, 242501 (2001).
[25] A. Kievsky, E. Pace, and G. Salmè, Eur. Phys. J. A **19**, Suppl. 1, 87 (2004).
[26] A. Deltuva, L. P. Yuan, J. Adam, Jr., and P. U. Sauer, Phys. Rev. C **70**, 034004 (2004).
[27] J. Arrington *et al.*, Phys. Rev. Lett. **82**, 2056 (1999), and references cited therein.
[28] E. Pace, G. Salmè, and G. B. West, Phys. Lett. **B273**, 205 (1991).
[29] O. Benhar, Phys. Rev. Lett. **83**, 3130 (1999), and references cited therein.
[30] H. Arenhövel *et al.*, Few-Body Syst. **15**, 109 (1993).
[31] C. Ciofi degli Atti, E. Pace, and G. Salmè, Phys. Rev. C **43**, 1155 (1991).
[32] T. W. Donnelly and A. S. Raskin, Ann. Phys. (NY) **169**, 247 (1986).
[33] A. Kievsky, E. Pace, G. Salmè, and M. Viviani, Phys. Rev. C **56**, 64 (1997).
[34] C. Ciofi degli Atti, S. Scopetta, E. Pace, and G. Salmè, Phys. Rev. C **48**, R968 (1993).
[35] C. Ciofi degli Atti, E. Pace, and G. Salmè, Phys. Rev. C **51**, 1108 (1995).
[36] R.-W. Schulze and P. U. Sauer, Phys. Rev. C **48**, 38 (1993).
[37] H. Hajduk-Meier *et al.*, Nucl. Phys. **A395**, 332 (1983).
[38] R. B. Wiringa, V. G. J. Stoks, and R. Schiavilla, Phys. Rev. C **51**, 38 (1995).
[39] G. Höhler *et al.*, Nucl. Phys. **B114**, 505 (1976).
[40] J. Carlson and R. Schiavilla, Rev. Mod. Phys. **70**, 743 (1998).
[41] S. Ishikawa, H. Kamada, W. Glöckle, J. Golak, and H. Witała, Nuovo Cimento **107A**, 305 (1994).
[42] S. Ishikawa, J. Golak, H. Witała, H. Kamada, W. Glöckle, and D. Huber, Phys. Rev. C **57**, 39 (1998).
[43] D. O. Riska, Phys. Scr. **31**, 107 (1985); **31**, 471 (1985).
[44] R. Machleidt, in *Advances in Nuclear Physics*, edited by J. W. Negele and E. Vogt (Plenum Press, New York, 1989), Vol. 19, pp. 189–376.
[45] J. L. Friar, B. F. Gibson, G. L. Payne, A. M. Bernstein, and T. E. Chupp, Phys. Rev. C **42**, 2310 (1990).
[46] J. Golak, W. Glöckle, H. Kamada, H. Witała, R. Skibinski, and A. Nogga, Phys. Rev. C **65**, 044002 (2002).
[47] R. Alley *et al.*, Nucl. Instrum. Methods A **365**, 1 (1995).
[48] R. Prepost and T. Maruyama, Annu. Rev. Nucl. Part. Sci. **45**, 41 (1995).
[49] J. Alcorn *et al.*, Nucl. Instrum. Methods A **522**, 294 (2004).
[50] M. A. Bouchiat, T. R. Carver, and C. M. Varnum, Phys. Rev. Lett. **5**, 373 (1960).
[51] J. S. Jensen, Ph.D. thesis, California Institute of Technology, 2000.
[52] I. Kominis, Ph.D. thesis, Princeton University, 2001.
[53] W. Xu, Ph.D. thesis, Massachusetts Institute of Technology, 2002.
[54] I. V. Akushevich and N. M. Shumeiko, J. Phys. G **20**, 513 (1994).
[55] J. Schwinger, Phys. Rev. **75**, 898 (1949).
[56] A. Amroun *et al.*, Nucl. Phys. **A579**, 596 (1994); C. R. Otterman *et al.*, *ibid.* **A435**, 688 (1985); P. C. Dunn, S. B. Kowalski, F. N. Rad, C. P. Sargent, W. E. Turchinetz, R. Goloskie, and D. P. Saylor, Phys. Rev. C **27**, 71 (1983) .
[57] O. N. Ozkul, Senior thesis, Massachusetts Institute of Technology, 2000.
[58] F. Xiong, Ph.D. thesis, Massachusetts Institute of Technology, 2002.
[59] A. Amroun, V. Breton, J. M. Cavedon, B. Frois, D. Goutte, J. Martino, X. H. Phan, S. K. Platchkov, I. Sick, and S. Williamson, Phys. Rev. Lett. **69**, 253 (1992).
[60] F. Ritz, H. Göller, T. Wilbois, and H. Arenhövel, Phys. Rev. C **55**, 2214 (1997).
[61] S. Jeschonnek and T. W. Donnelly, Phys. Rev. C **57**, 2438 (1998).
[62] T. W. Donnelly (private communication).
[63] J. A. Caballero, T. W. Donnelly, and G. I. Poulis, Nucl. Phys. **A555**, 709 (1993).
[64] T. de Forest *et al.*, Nucl. Phys. **A392**, 232 (1983).
[65] H.-W. Hammer and Ulf-G. Meißner, Eur. Phys. J. A **20**, 469 (2004).
[66] G. Holzwarth, talk at the Workshop on Nucleon Form Factors, Frascati, 12–14 October 2005; see also Z. Phys. A **356**, 339 (1996) and hep-ph/0201138.
[67] B. Kubis and U.-G. Meissner, Nucl. Phys. **A679**, 698 (2001).
[68] E. L. Lomon, Phys. Rev. C **66**, 045501 (2002).
[69] J. P. B. C. de Melo, T. Frederico, E. Pace, S. Pisano, and G. Salmè, Nucl. Phys. **A782**, 69c (2007).